



Effects of lead and lean in multi-axis directed energy deposition

Omar Elsayed¹ · Venkata Surya Karthik Adapa¹ · Samuel Kersten¹ · Derek Vaughan¹ · Christopher Masuo¹ · Myong Joon Kim¹ · Thomas Feldhausen² · Christopher Saldana¹ · Thomas Kurfess¹

Received: 27 November 2022 / Accepted: 7 February 2023 / Published online: 13 February 2023
© The Author(s), under exclusive licence to Springer-Verlag London Ltd., part of Springer Nature 2023

Abstract

The present study examines the effect of varying laser incidence angles on textural, microstructural, and geometric characteristics of directed energy deposition (DED) processed materials, providing a more comprehensive outlook on participating laser-matter interaction phenomena and ultimately devising strategies to ameliorate print performance. In this study, single-layer, single-/multi-track specimens were processed to examine the effect of non-orthogonal angular configurations on bead morphology, microstructure, phase composition, and textural representation of DED-processed 316L stainless steel materials. It was observed that bead size decreased at increasing lead and lean angles. Asymmetry in the distribution of the bead morphology as a function of lead angle indicates better catchment for acute lead angle configurations over obtuse configurations. No significant differences in phase composition, texture, and microstructure were observed in moderate off-axis configurations. When the penetration depth for the deposits was below 20 μm , columnar structures dominated the microstructure of the deposited material. At deeper penetration depths, columnar and equiaxed structures were observed at the bead-substrate interface and center of the bead, respectively. Compared to powder-blown DED, wire-DED dilution profiles were found to be asymmetric in both orthogonal and non-orthogonal wire DED samples.

Keywords Directed energy deposition · Additive manufacturing · Microstructure

✉ Venkata Surya Karthik Adapa
karthik.adapa@gatech.edu

Omar Elsayed
oelsayed791@gmail.com

Samuel Kersten
skersten3@gatech.edu

Derek Vaughan
dvaughan3@gatech.edu

Christopher Masuo
cmasuo3@gatech.edu

Myong Joon Kim
mkim3@gatech.edu

Thomas Feldhausen
feldhausenta@ornl.gov

Christopher Saldana
christopher.saldana@me.gatech.edu

Thomas Kurfess
kurfess@gatech.edu

¹ George W. Woodruff School of Mechanical Engineering, Georgia Institute of Technology, 801 Ferst Dr, Atlanta, GA 30332, USA

² Manufacturing Automation and Controls Group, Oak Ridge National Laboratory, Oak Ridge, TN 37831, USA

1 Introduction

Hybrid manufacturing is an emerging technology that incorporates both additive and subtractive manufacturing (AM and SM, respectively) in producing net-shape components, yielding advantages that neither technology can supply when used in isolation [1–3]. By combining additive and subtractive capabilities, components with complex geometries can be manufactured and post-processed to produce dimensional accuracies and surface finishes that are unmatched by using current additive or subtractive technologies alone, all in one unified machine [4, 5]. Complex geometries produced by hybrid manufacturing generally require the use of off-axis tool orientation (e.g., lead and lean) to accommodate reach and access to manufacture specific component geometry. When dealing with highly intricate geometries in hybrid manufacturing, the issues that arise due to tool reachability and access in both additive and subtractive steps of the process become significant, increasing the probability of tool crashing dramatically.

The impact of off-axis deposition orientation in DED has not been well established. In DED, a conical nozzle outputs powder at an angle, allowing powder to meet the focused laser beam at the workpiece surface. During deposition, however, not all the deposited powder is melted; rather, random, and turbulent rebounding of the powder particles results in a powder cloud [6]. As these particles get exposed to the laser beam, they absorb and/or reflect some of the laser energy [7]. In low-melting and boiling-point alloy deposition, vapor plumes exacerbate this optical obstruction [8]. As a result, the effective laser energy used to create the melt pool is lower than intended. This is referred to as laser attenuation and can result in considerable efficiency losses. The laser incidence angle can have a direct effect on the extent of laser attenuation and can be strategically employed to reduce efficiency losses that are endemic to more extreme process parameters. Various theoretical models and experimental validations were conducted to analyze the effects laser attenuation has on deposition performance when laser incidence angle is varied. Fu et al. developed a theoretical model where it was observed that increasing angle between the laser and powder jet incident angles resulted in more asymmetric temperature distributions as well as lower average temperatures due to the reduced travel experienced by the particles within the laser field [9]. It was also observed that laser attenuation increased on decreasing angles between laser and powder jet incidence angles, resulting in upwards of 50% effective power losses and transforming the power distribution from Gaussian to non-Gaussian in nature. Liu et al. have also shown that laser attenuation is enhanced with increasing particle feed rate and particle speed, with up to 10% efficiency losses [10]. Pinkerton et al. found that laser attenuation becomes significantly more pronounced once the powder streams converge to form a single stream at the center [11]. The laser incidence angle can also directly affect the resultant print bead morphologies. Hao et al. [12] observed that an increasing laser-to-substrate angle (lead angle) results in an increasing bead width and peak point shifting. This was attributed to the presence of gravitational effects and/or changes in spot size and geometry.

There have been various efforts to examine the effect of laser incidence angles on printing performance, including characteristics such as bead geometry and laser power/surface temperature distributions, amongst others [10–12]. However, limited work has

been conducted on examining the effect of laser incidence angles on bead texture and microstructure. Furthermore, no work has been done to relate such domains with bead geometry, laser attenuation, or other participating physical phenomena to provide a more holistic understanding of some underlying laser-matter interaction phenomena in directed energy deposition processes. To address this need, the present study seeks to understand the impact of laser incidence angle in DED on bead morphology, microstructure, and texture, as well as the nature of its effects. In addition, a comparison study is also required to understand the impact of laser incidence angle in the powder feed against wire feed DED methods. Typically, a wire DED system has nearly 100% feedstock catchment efficiency, significantly higher than the powder feed system due to no bombardment of powder particles. With an expectation that wire feed DED exhibits a prominent trend, a similar microstructural characterization study, including the bead morphology, is investigated to assess and understand the similarities between powder and wire feed DED systems.

2 Experimental procedure

Powder-blown DED was employed to perform the required experiments in this study using the Mazak VC-500AM hybrid machine, equipped with an Nd-YAG laser (1064 nm) and a coaxial nozzle setup typically allows X degrees of maximum angle of deposition. The powder material of choice was 316L austenitic stainless steel (sourced from LPW Technology Limited, a Carpenter Company). The 316L powder material was deposited on a 316L substrate with a thickness of 6.35 mm, and the chemical composition of the powder material is provided in Table 1. The particle size distribution of the powder used in this study was within 45–106 μm , per the sieve analysis conducted following ASTM-B214. The process parameters used in this experimentation were kept constant to isolate the effects of incidence angle on phase composition, texture, bead morphology, and microstructure. Table 2 illustrates the parameters used for this process that yields more than 99% dense material for 316L.

The angle between the laser head's vertical axis and the workpiece surface is known as the laser incidence angle.

Table 1 316L austenitic stainless steel chemical composition (wt%) (sourced from LPW Technology Limited, a Carpenter Company)

Fe	Cr	Ni	Mo	Mn	Si	N	C	Cu	O	P	S
Bal.	17.8	13.0	2.40	1.04	0.64	0.1	0.02	0.02	0.01	0.01	0.004

Table 2 Powder-feed DED process parameters

Parameter	Value
Laser spot diameter (mm)	1
Scanning speed (mm/min)	300
Laser power (W)	400
Nozzle gas flowrate (L/min)	2
Shielding gas flowrate (L/min)	10
Carrier gas flowrate (L/min)	5
Powder feed rate (g/min)	4.6

Table 3 Experiment 1 angular configurations

Configuration	Lead angle θ ($^{\circ}$)	Lean angle β ($^{\circ}$)
Orthogonal	90	0
Pure lean	90	15, 30
Pure lead	45, 60, 75, 105, 120, 135	0
Compound	45, 60, 75, 105, 120, 135	15, 30

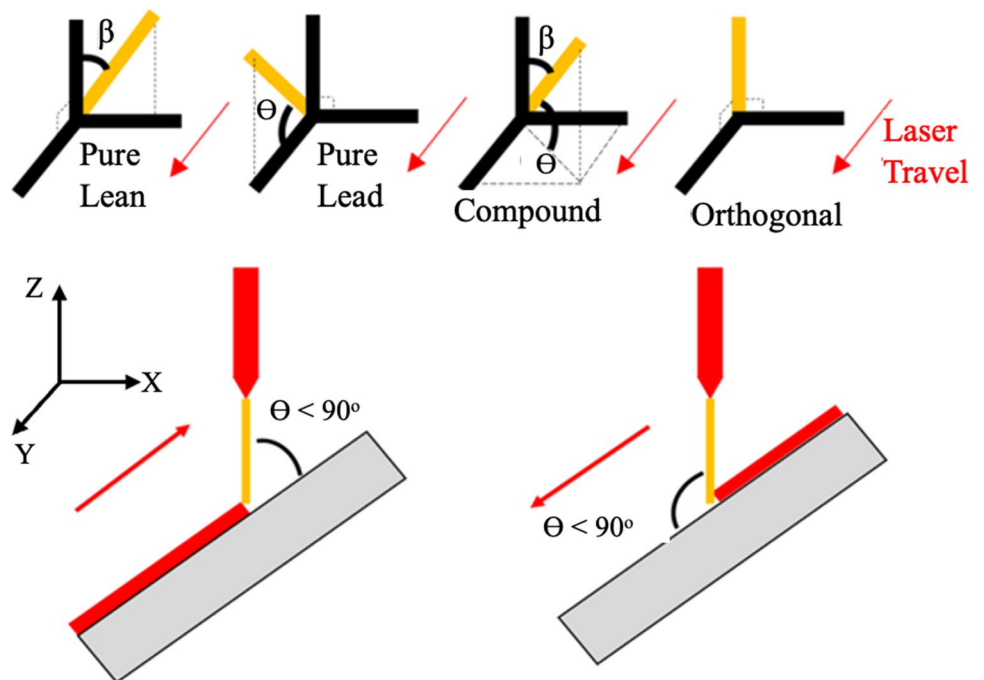
In terms of deposition, there are two types of incidence angles: lead and lean. The lead angle is the angle produced in the YZ plane (also known as the tilt angle [12]), while the lean angle is the angle produced in the XZ plane (assuming the laser travels in the Y-direction). In general, there are four main configurations possible: orthogonal, pure lean/lead, and compound lean/lead angles. Figure 1 visually illustrates the differences between the various angular configurations discussed here. The yellow line represents the laser beam, while the coordinate system shown is that of the substrate.

The effects of pure lead, pure lean, compound, and orthogonal angle on bead geometry were evaluated. A set of 5 long, single-layer, single-track depositions are conducted for each configuration. The various angular configurations examined are shown in Table 3. The samples are deposited approximately 5 mm apart to prevent heat-affected zone (HAZ) overlapping, which

can interfere with the melt-pool and solidification dynamics as well as the resultant microstructure of the deposits. A single-layer track was employed to avoid altering melt-pool behaviors and introducing secondary effects of vertical inter-layer diffusion and solidification phenomena, therefore convoluting the primary results of this study. After deposition, the samples were sectioned and mounted for metallographic examination to examine bead geometry via optical microscopy. Five samples of each configuration were obtained. A 3:2:1-part solution of distilled water, hydrochloric acid, and nitric acid is used to reveal the bead cross-sections here (Solution 88 from ASTM E407-99). The evaluation metrics in this experiment were bead height, bead width, and penetration depth (the maximum distance penetrated by the laser to induce dilution in the substrate).

Differences in phase composition and texture were evaluated between non-orthogonally (pure lead configurations of $\theta = 60$ and 120°) deposited material, orthogonally deposited material, and the raw,

Fig. 1 Top: orthogonal and non-orthogonal angle representations. Bottom: lead angle deposition techniques



unprocessed powder. In this experiment, three 1×0.5 in, single-layer, multi-track samples were produced: a sample with an orthogonal configuration and two samples with pure lead angles of $\theta = 60$ and 120° . A single-layer track was employed to avoid altering melt-pool behaviors and introducing secondary effects of vertical inter-layer diffusion and solidification phenomena, therefore convoluting the primary results of this study. A multi-track deposit was necessary due to spot size limitations set forth by the X-ray equipment utilized in this experiment. Phase analysis was conducted on all three samples as well as the raw, unprocessed powder to provide a comparative basis on the processing effects on phase composition. Textural analysis was then conducted to obtain orientation distribution functions (ODF) to map the textural demographics present in the samples. The orientation distribution functions provide a global representation of texture within a large area of a sample, thus providing a higher-level view of the crystallographic orientations in the investigated samples.

The effects of pure lead, pure lean, and compound angle on microstructure were evaluated. A set of 1 in single-track, single-layer samples with various angular configurations was deposited, as shown in Table 4. They were then sectioned and prepared for detailed microstructural analysis. The grain size was also

examined in 7 different 100 by $100 \mu\text{m}$ regions that cover the entirety of the bead, as shown by the green boxes in Fig. 2. Five straight, horizontal lines were drawn at equal intervals within the square region on the optical micrographs, and the line intercept method was used [13]. Grain sizes are then compared both between regions within a bead and across beads. Furthermore, a set of 4 samples of extreme non-orthogonal deposition angles was also investigated to examine the effect of extreme non-orthogonal, compound angle deposition on bead microstructure. The angular configurations examined here are presented in Table 4.

A Macken Instruments P2000Y laser power probe was used to quantitatively measure the effects of varying incidence angles on the effective power reaching the substrate surface [14]. Angular configurations examined are denoted in Table 1. A stand-off distance of 33 mm was maintained to ensure the laser spot size was larger than the minimum manufacturer recommendation of 1.09 cm to prevent equipment damage. The power probe was exposed to the laser beam for 21 s per run, as per manufacturer instructions. To accomplish this, the probe is rotated in such a way that a full rotation is complete in 21 s. The circular trajectory of the laser beam had a diameter of 31 mm, so the linear travel speed was 300 mm/min. The experiments are run with the powder feed on and off to attempt at decoupling laser spot size and powder attenuation effects, respectively. Figure 3 illustrates the experimental setup used here. The power absorbed by the power meter (termed the effective power here) was compared to the command power (set at 400 W for this study) to obtain the difference in power, representing the power loss experienced as the laser travels to the substrate.

$$P_{\text{effective}} = P_{\text{command}} - P_{\text{attenuated}}$$

Table 4 Experiment 3 angular configurations

Configuration	Lead angle θ ($^\circ$)	Lean angle β ($^\circ$)
Orthogonal	90	0
Pure lean	90	15
Pure lead	75, 105	0
Compound	75, 105	15
Upper and lower bounds	45, 135	15, 45

Fig. 2 Lead angle effects on bead microstructure experimental setup. Left: cross sectional area to be investigated metallographically. L, left; C, center; TC, top center; TR, top right; BL, bottom left; BC, bottom center; BR, bottom right. Right: examined region for the manual intercept method setup

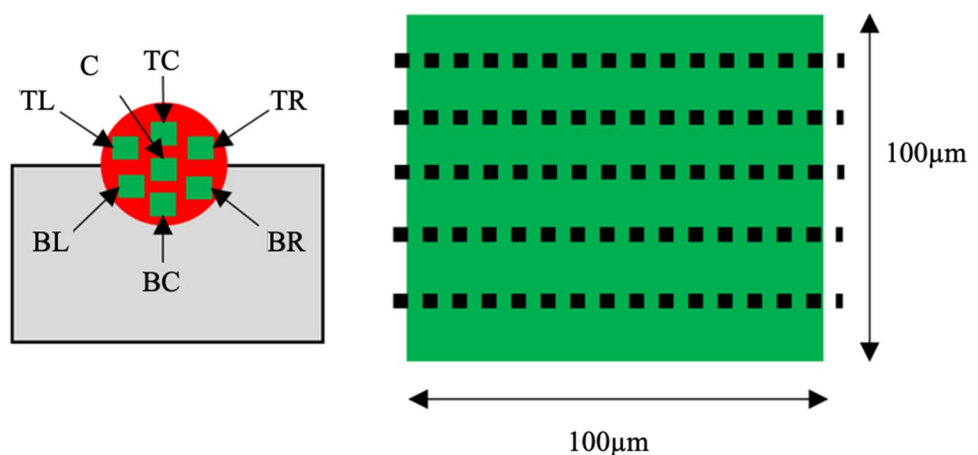


Fig. 3 Laser power measurement experimental setup (top right figure obtained from the manufacturer’s website [L])

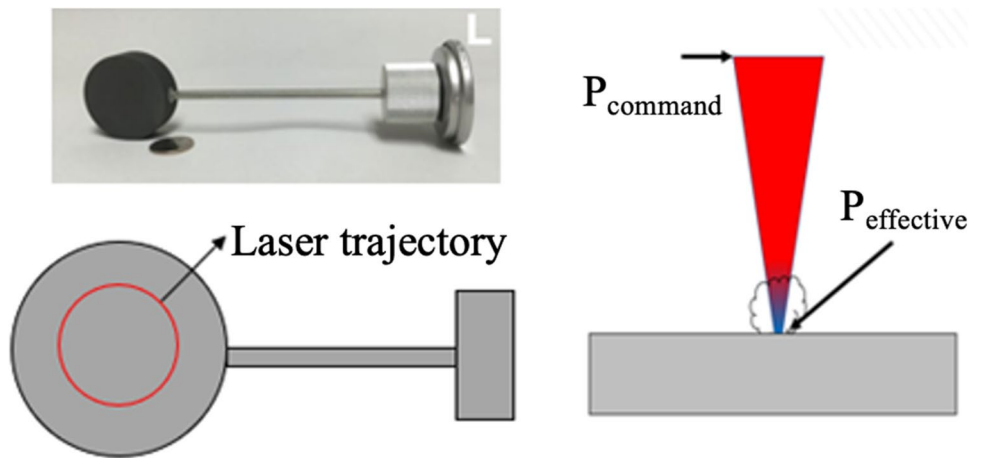


Table 5 Experiment 5 angular configurations

Angular configuration	Lead angle θ (°)	Lean angle β (°)
Orthogonal	90	0
Pure lean	90	15, 30, 40
Pure lead	60, 75, 90, 105, 130	0

Table 6 Wire-feed DED process parameters

Process parameter	Value
Laser spot diameter (mm)	3
Scanning speed (mm/min)	1067
Laser power (W)	2750
Nozzle gas flowrate (L/min)	20
Shielding gas flowrate (L/min)	20
Wire feed speed (mm/min)	4445
Hot wire power (W)	420

Finally, a comparative study using the Mazak VC-500A/5X AM HWD system to compare the non-orthogonal deposition performance of powder-feed and wire-feed hybrid AM systems. The specific lean and lead angles examined in this experiment are shown in Table 5, where the angular configurations used are limited by the physical nature of the wire-DED setup. The more extreme angular configuration used in powder DED can result in a nozzle—workpiece contact in a wire DED system. The wire-fed samples are processed using a 3-kW continuous wave (CW) laser. A 0.045 in (1.14 mm) 316L SS wire was used as the wire gauge and material of choice, respectively. The process parameters used are summarized in Table 6. Optical microscopy

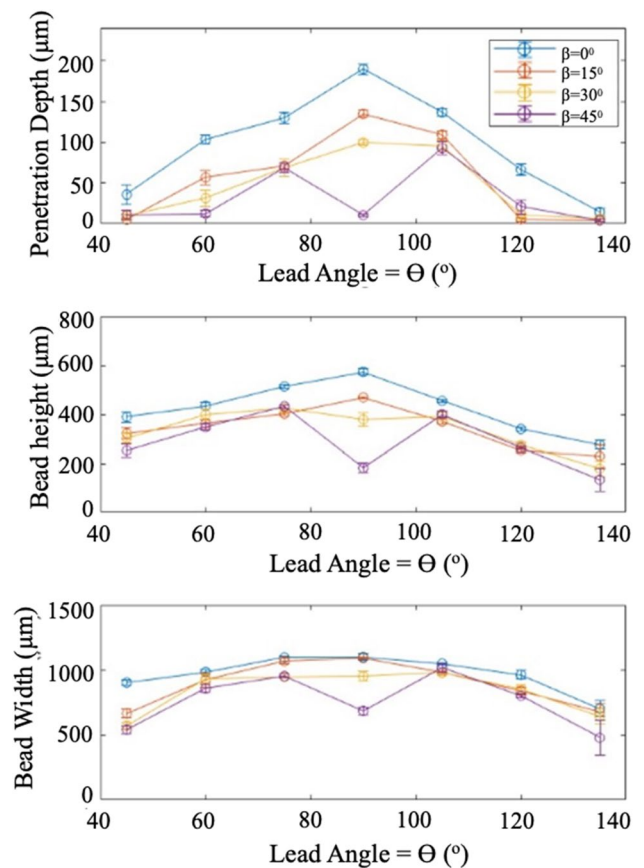


Fig. 4 Lean and lead angles effects on bead morphology. Normal curve behavior with more extreme lead angles. Diminishing parameters with more extreme lean angles

was then employed to examine the geometric and microstructural characteristics of the resultant bead cross-sections. More specifically, bead height, width, penetration depth, and grain structure are studied.

3 Results

3.1 Effects of lead and lean angles in blown powder DED

Figure 4 illustrates the resultant bead widths, heights, and penetration depths of the various angular configurations examined on multiple cross-sections from each specimen, and the standard deviation is represented as an error bar. From the figure, an increase in lean angle resulted in diminished penetration depth, bead height, and bead width, irrespective of the lead angle utilized. Penetration depth experienced a more significant drop with a 75° lead angle as compared to a 105° lead angle. However, with more extreme lead angles, obtuse lead angle penetration depths decreased more significantly, with penetration depths highly dependent on a lean angle here, as observed by the spread in the data. Another observable asymmetry can be seen in the bead height changes, where bead height was lower in lead angle configurations higher than 90° for all lean angles used compared to their mirror equivalents under 90° . Regarding bead width, slight asymmetry was observed when comparing acute and obtuse lead angles, with acute lead angle bead widths having slightly higher values than obtuse lead angle bead widths, especially for lower lean angle compound configurations. Interestingly, across all bead parameters examined, incorporating a pure lean angle of 45° resulted in a pronounced drop in bead height, width,

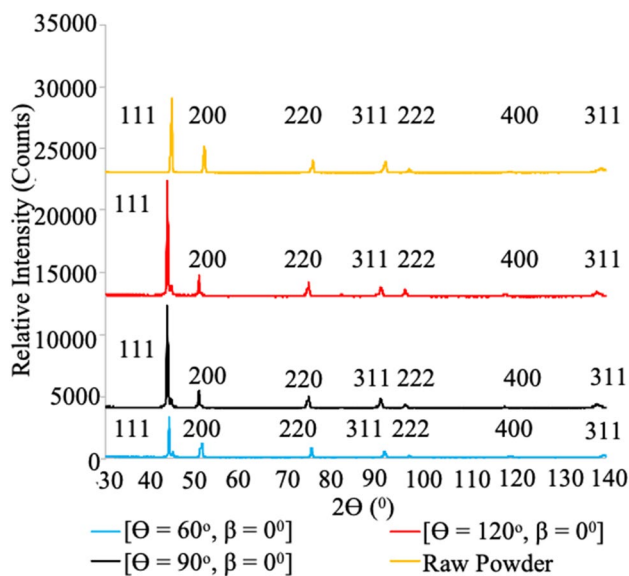


Fig. 5 X-ray diffraction peak patterns. Yellow: raw, unprocessed powder. Red: $\theta = 120^\circ$ pure lead condition. Black: orthogonal sample. Blue: $\theta = 60^\circ$ pure lead condition. No significant differences in phases were observed

and penetration depth as compared to its compound angle counterparts.

Figure 5 illustrates the X-ray diffraction peaks of the non-orthogonal and orthogonal configurations as well as that of the unprocessed powders. The diffraction peaks were overlaid for ease of visualization. The material candidates that matched the unprocessed and processed samples (C–Cr–Fe–Ni and $\text{CFe}_{15,1}$) were austenitic FCC phases. From the figure, no relative differences were detected in peak locations. The qualitative austenitic FCC phase determination was sufficient for subsequent analyses, which were highly dependent on the h-k-l values representative of the detected peaks at lower angles.

Figure 6 illustrates the calculated orientation distribution functions of the non-orthogonal and orthogonal processed samples. From the texture measurements conducted, it was observed that similar textural representations were present in orthogonal and non-orthogonal samples. The significant texture was observed at $\varphi = 60^\circ$, $\varphi_2 = 45^\circ$, and all φ_1 values for all the samples, indicating that fiber texture is dominant in this specific orientation. Furthermore, high texture intensities were observed in the $\varphi_2 = 15^\circ$ and $\varphi_2 = 75^\circ$ plots around $\varphi = 75^\circ$ in various φ_1 angles, as observed in the figures. The remaining areas in the ODFs exhibited little texture elsewhere, confirming that a significant textural representation is indeed present, as observed by the high intensity counts in the diffraction patterns in Fig. 5.

Figure 7 illustrates the grain size differences between the various regions within a specific sample and across different samples for pure lead angle and pure lean/compound angle configurations. The data is divided into two plots: a pure lead condition ($\beta = 0^\circ$) and a compound condition ($\beta = 15^\circ$). All seven regions selected to examine the microstructure within each plot are illustrated and separated from each other as shown. Within each region of the plots, the various angular configurations are situated side-by-side for an easy-to-visualize comparison. As observed in Fig. 7, minor microstructural grain size variations were observed with changing lead and lean combinations across samples, with variations not exceeding 1–1.5 μm . Furthermore, variations between neighboring regions within a sample did not exceed 2–2.5 μm . Nevertheless, the grains nearest to the center were slightly smaller than on the outer edges of the bead. Figure 8 illustrates the micrographs obtained from pure lean, pure lead, compound, and orthogonal angular configurations. Similar solidification fronts were observed in all samples. They all exhibited a radial symmetry, which originated in the top center

region of the beads. Columnar structures were detected at the outer edges of the bead, more specifically at the bead-substrate interface, while more equiaxed and cellular structures were observed closer to the center of the beads, as shown in Fig. 9. For beads with very shallow penetration depths ($< 20 \mu\text{m}$, more apparent in more extreme lead angles of 45 and 60° , as shown in Fig. 4), columnar structures dominated the general microstructure, with little to no equiaxed or cellular structures present. This is depicted in Figs. 9 and 10.

Figure 11 illustrates the laser power measurements obtained from this experiment. A dioptric power loss of approximately $25\text{--}50 \text{ W}$, representing a 6.25 to 12.5% drop from the command power of 400 W , was observed when the machine was operated with the powder feed turned off. Regarding the effect of varying the incidence angles, the consequential laser spot size changes that were experienced did not have a specific effect on the amount of power reaching the probe surface. No observable trend was seen in the obtained results, with most data points lying within a 25 W range between 350 and 375 W . The measured power was, on average, approximately $362.5 \pm 12.5 \text{ W}$ for all measured incidence angle combinations. When the powder feed was turned on, the measured laser power dropped an additional $25\text{--}50\text{W}$, resulting in an 18.75 to 25% overall drop from the command power of 400 W . When the powder feed was off, changing the laser incidence angle configuration did not significantly affect the power measured/absorbed by the probe. The measured power here was, on average, approximately $315 \pm 10 \text{ W}$ for all measured incidence angle combinations.

3.2 Effects of lead and lean angles in wire-fed DED

Figure 12 illustrates the bead cross-sectional micrographs obtained from the pure lead (A, B, D, and E), pure lean (F, G, and H), and orthogonal (C) angle depositions in the wire feed DED case. Figure 12A, B, C, D, E, F, G, and H show that the dilution region is asymmetrically positioned away from the bead center. In pure lead angle configurations (except for $[\theta = 105^\circ, \beta = 0^\circ]$ in 12D), the dilution region was preferentially positioned to the right of the bead center, with no significant variations in position with increasing lead angles. In pure lean angle configurations, the dilution region was preferentially positioned to the left of the bead center, progressively shifting to the right with increasing lean angle. An asymmetry was also observed in the orthogonal configuration.

As compared to other angular configurations, the $[\theta = 105^\circ, \beta = 0^\circ]$ pure lead angle configuration (Fig. 12D) exhibited a much smaller and distinctive penetration depth profile. Maximum penetration was observed toward the bead extremities (compared to a preferentially centered, though asymmetric location for other angular configurations).

The relation between angular configuration and bead geometry (bead height, width, and penetration depth) is illustrated in Fig. 13. It can be observed in Fig. 13A and B that height and penetration depth followed an inverse Bell curve relationship with increasing lead angles. On the other hand, Fig. 13C shows that bead width exhibits a normal Bell curve behavior. A noticeable asymmetry in bead geometry changes due to angular configuration can be observed in lead angles lower than 105° as compared to lead angles larger than 105° . Penetration depth and bead height exhibit a Bell curve behavior, with maximum penetration depth and maximum bead height experienced at $\beta = 30^\circ$ and $\beta = 15^\circ$, respectively. Bead width experiences an inverse Bell curve behavior, with the minimum width experienced at $\beta = 15^\circ$. At $\beta = 40^\circ$, a significant jump in bead width was experienced.

Figure 14A illustrates the microstructure of the $[\theta = 105^\circ, \beta = 0^\circ]$ pure lead sample. Fig. 14B–D show higher magnification images of the top, bottom, and center of the bead to examine the bead's solidification fronts. Columnar and equiaxed dendrites separated by columnar to equiaxed transition (CET zones) are observed. Fine columnar dendrites were observed predominantly toward the center of the beads, as shown in Fig. 14D. On the other hand, these columnar dendrites transition to equiaxed dendrites around the bead edges, as shown in Fig. 14B and C.

4 Discussion

As shown in Fig. 4, penetration depth experienced a drop with exceedingly non-orthogonal configurations, which can be due to the absolute distance traveled by the laser into the substrate. In an orthogonal setting, the penetration depth is at its maximum. However, with exceedingly non-orthogonal configurations, the laser travel trajectory is increasingly diagonal to the substrate surface, resulting in a reduced absolute penetration depth. Such phenomena have been observed in pulse laser welding of stainless steel [15]. This can be advantageous since this can reduce the remelted and recrystallized regions in previously deposited layers,

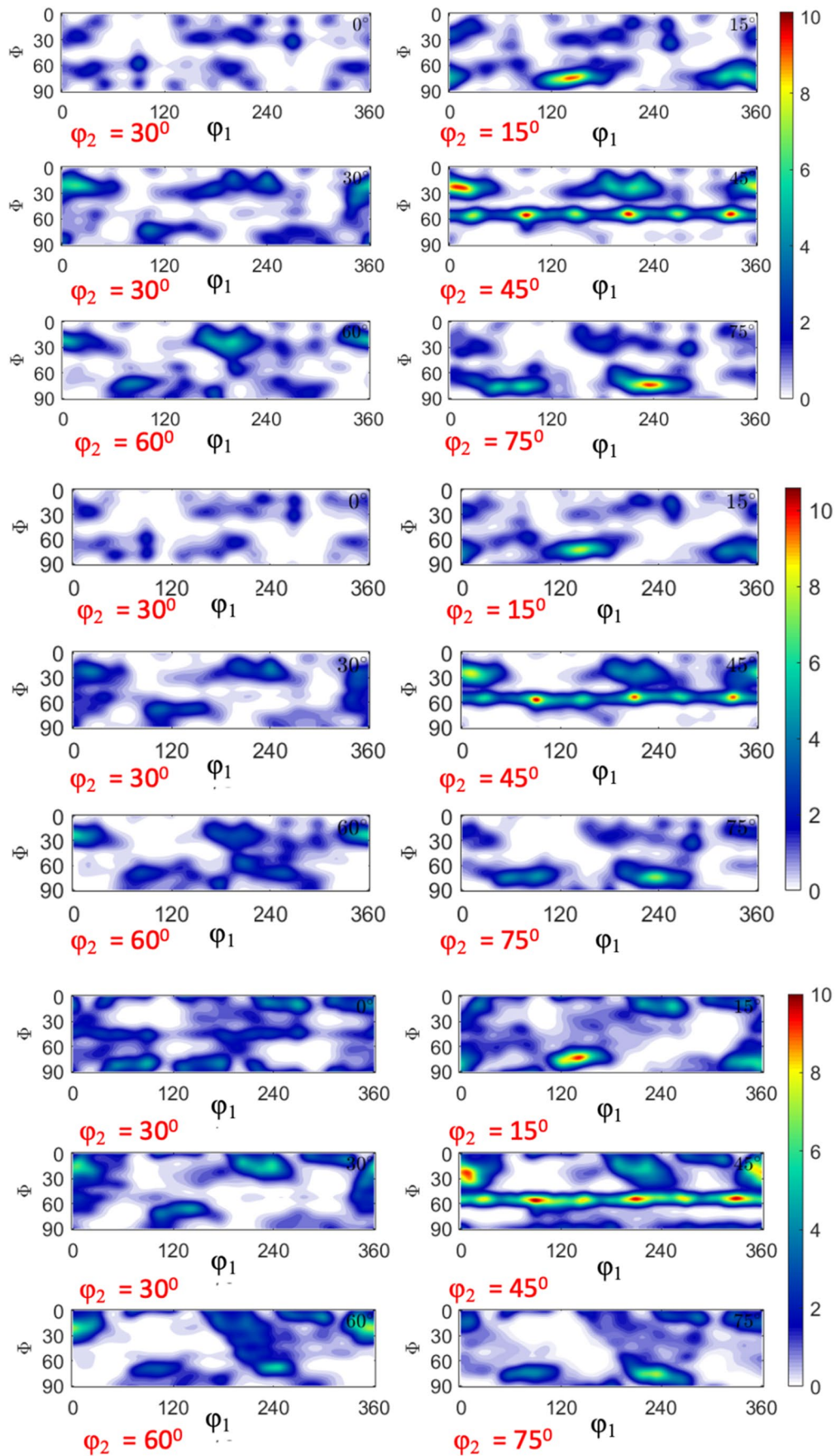


Fig. 6 Orientation distribution function plots. Top: $\theta = 60^\circ$; $\beta = 0^\circ$. Middle: $\theta = 90^\circ$; $\beta = 0^\circ$. Bottom: $\theta = 120^\circ$; $\beta = 0^\circ$. No significant differences in textural representation between samples

resulting in a less complex/involved thermal history for the deposited material. The observed asymmetry, especially in less extreme non-orthogonal deposition samples, can indicate the presence of some of the underlying heat transfer phenomena. For acute lead angles, the laser power not only transfers to the substrate but also to the previously deposited material, thus dissipating the effective energy reaching the surface to a larger volume as compared to the obtuse lead angle deposition samples, which have the laser power mainly transferring to the substrate (refer to Fig. 1 for better visualization).

Bead height and width also experienced a drop with more extreme non-orthogonal deposition, as shown in Fig. 4. Powder catchment efficiency seemed to play an integral role here. During deposition, powder particles hit the melt pool and float momentarily before melting [16]. With a continuous powder flow, a large number of particles impact the already floating particles, thus experiencing a ricochet effect. Therefore, the resultant partially and/or non-melted particles are the primary reason for spatter along deposition edges and powder cloud formations, respectively [17]. The bounce-back angle will depend on the impact angle, which depends on the coaxial nozzle design. However, with exceedingly non-orthogonal angles, the bounce-back angle increases, reducing the laser-matter interaction time and thus reducing powder catchment efficiency. The interaction time between the laser and the powder particles is directly related to the probability of these particles experiencing full, partial, or no melting. This outcome is primarily governed by the distance traveled within the laser's line of action. In other words, the longer a powder particle spends within the laser beam's line of action, the more energy it absorbs, and thus the propensity of its melting increases. For lead angles under 90° , as shown in Fig. 1, as the particles ricochet off the substrate, they are met with a "barrier" of the previously deposited material. As a result, some deflected particles are brought back into the melt pool, slightly enhancing powder catchment efficiency. This could explain the observed asymmetry in the results obtained.

For a pure lean angle of 45° , shown in Fig. 4, all bead metrics were the lowest, indicating that powder catchment efficiency was the least efficient in that

angular configuration. This can be due to the excessive ricochet effect that occurs here, especially at such an extreme angle. Austenitic FCC phases were observed in both processed and unprocessed samples, as expected. However, no other phases were detected in this experiment, as compared to the delta ferrite detected in Costello et al. [18]. This can be explained by the integral role the alloying elements play in austenite stabilization. Manganese content here was around 1 wt%, which, coupled with the ~ 18 wt% chromium presence, acts as an austenite stabilizer as compared to becoming a ferrite stabilizer in the 5–8 wt% range [19]. Furthermore, the presence of Ni in high concentrations ($\sim 13\%$) also promotes austenite stabilization. Thus, with the significant presence of austenite stabilizers, the presence of austenitic FCC phases seems valid in this experiment.

The diffraction peak patterns were equivalent, indicating that the general phase composition did not change with processing and varying angular configurations. Slight peak broadening was also observed, which can be attributed to the presence of residual stress (typically observed in additively manufactured materials), while the high peaks in the 111 and 200 planes point to textural representation within the material. The slight differences in diffraction patterns between the unprocessed and processed materials can stem from two possibilities. First, during processing, carbide and/or precipitate formations, which are common in 316L austenitic stainless steels, especially $M_{23}C_6$ carbides, could have occurred during the heating and re-heating of the material as one track is deposited next to the other to form the single layer [20]. Slight peak broadening was also observed, which can be attributed to the presence of residual stress, typically observed in additively manufactured materials, as well as the texture representation within the material.

The orientation distribution function results show that a visible fiber texture was present in the processed samples. Specifically, the fiber texture can be seen with consistently high intensities at $\varphi = 60^\circ$, $\varphi_2 = 45^\circ$, and all φ_1 values. This can represent the elongated columnar and dendritic formations that are endemic to the rapid solidification phenomena observed in this process. Some visible texture with high intensities was also present in the $\varphi_2 = 15^\circ, 45^\circ$, and 75° plots. These can represent the remainder equiaxed and cellular grain and sub-grain orientations that represent the general microstructural demographic of AM samples. Epitaxial growth can explain the reason behind the heavily fibrous texture

Fig. 7 Pure lead, lean and compound angle effects on grain size. **A** Pure lean (red) and compound (blue and yellow) angular configurations. **B** Pure lead (blue and yellow) and orthogonal (red) angular configurations. Negligible differences both between regions within a single bead and across beads for varying laser incidence angles

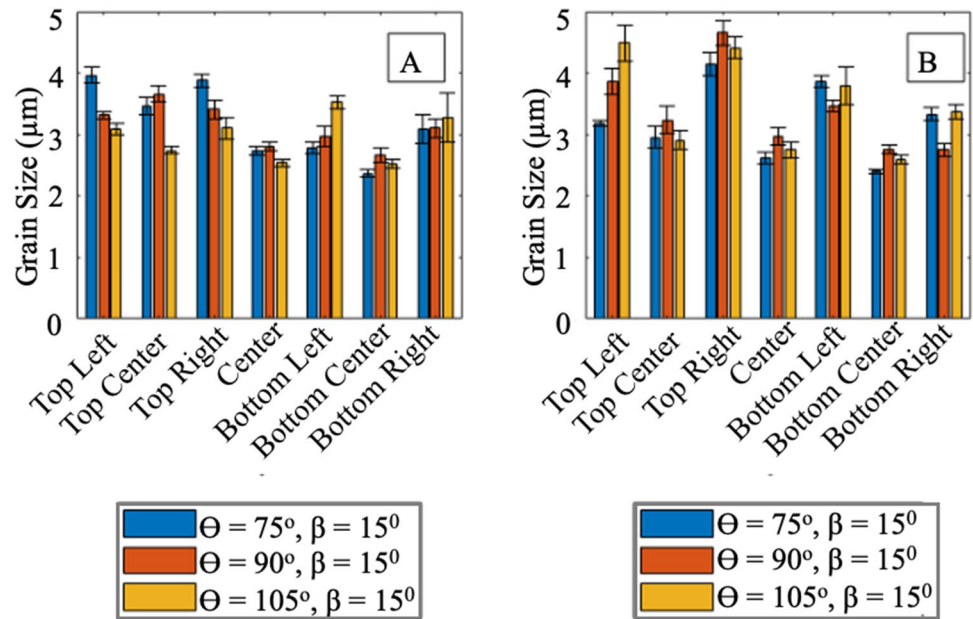


Fig. 8 Micrographs of orthogonal and non-orthogonal solidification fronts. **A** $\Theta = 75^\circ$; $\beta = 0^\circ$. **B** $\Theta = 90^\circ$; $\beta = 0^\circ$. **C** $\Theta = 105^\circ$; $\beta = 0^\circ$. **D** $\Theta = 75^\circ$; $\beta = 15^\circ$. **E** $\Theta = 90^\circ$; $\beta = 15^\circ$. **F** $\Theta = 105^\circ$; $\beta = 15^\circ$. Equivalent microstructural solidification fronts observed

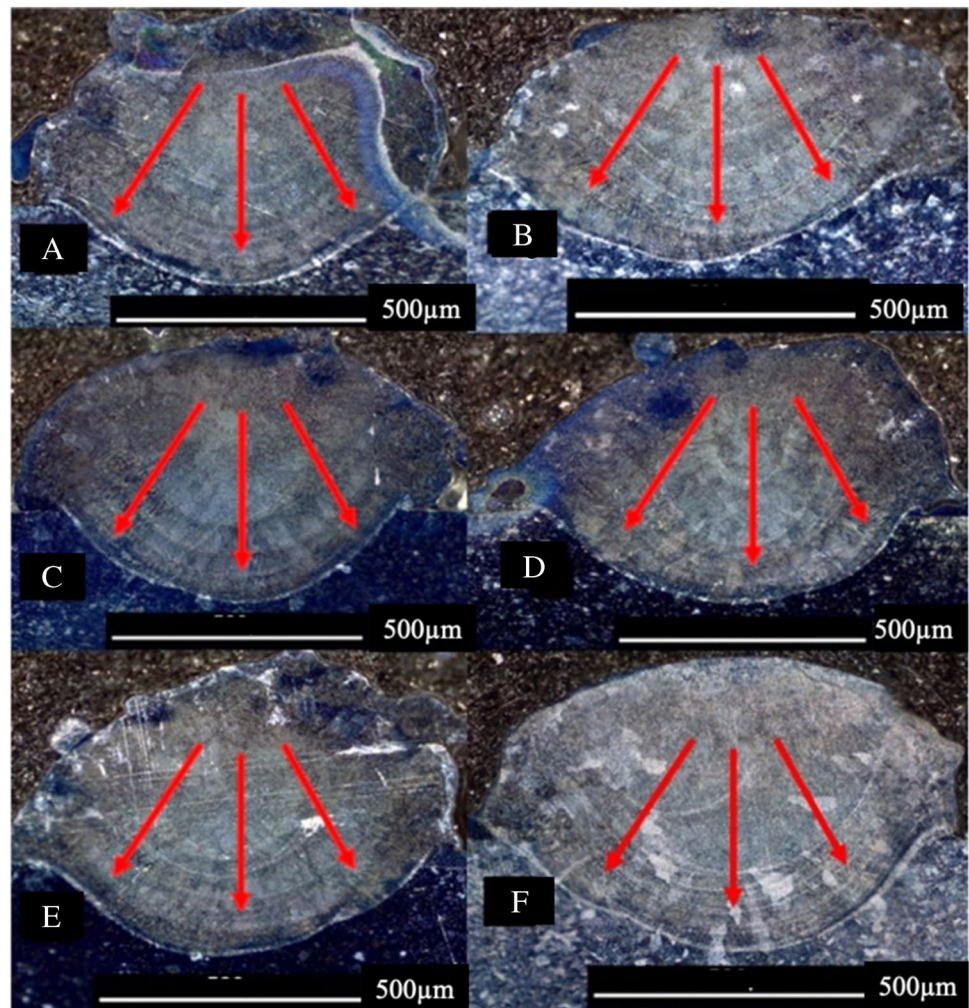
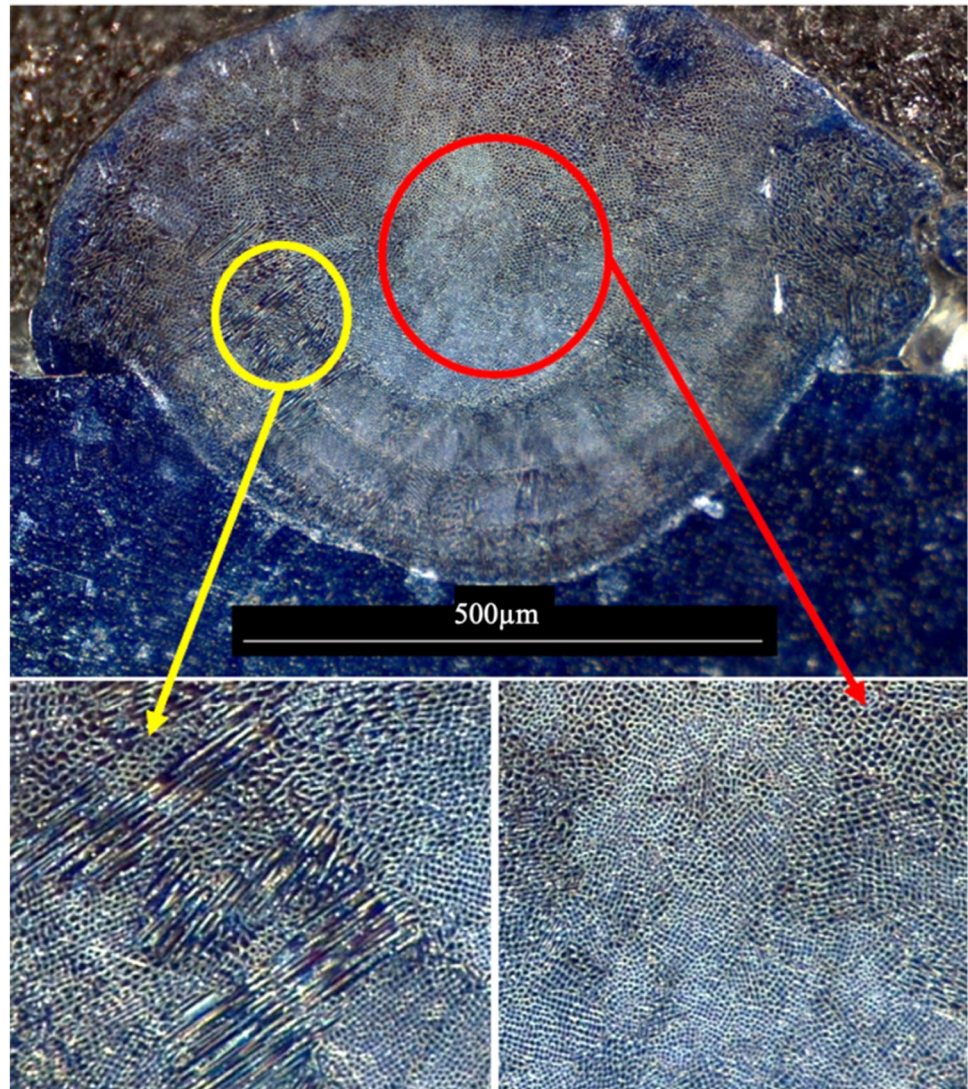


Fig. 9 Solidification microstructural observations in orthogonal and non-orthogonal bead depositions. Yellow: Columnar structures. Red: Equiaxed/cellular structures



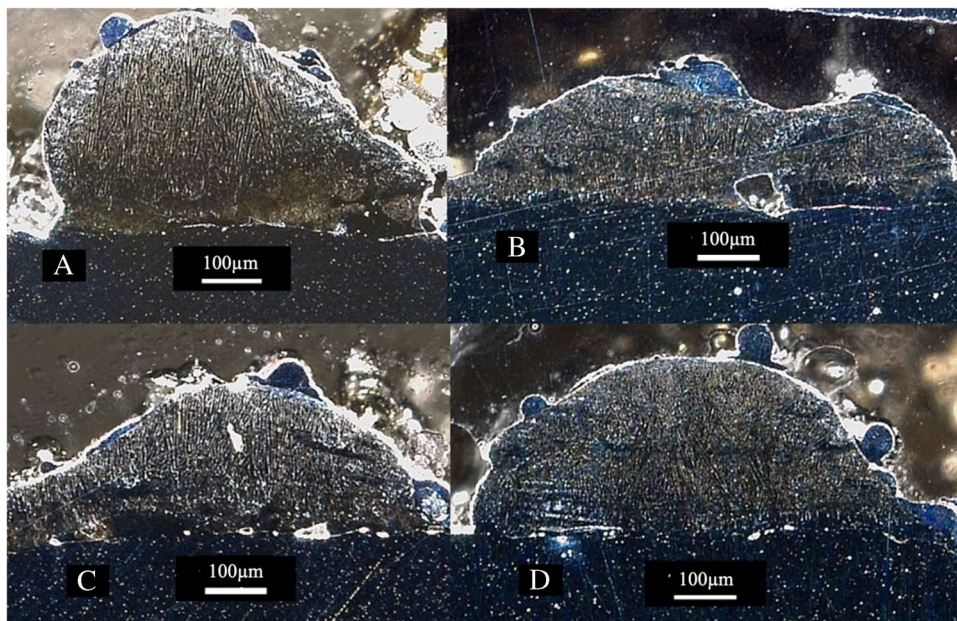
representation observed in this process, and this has been usually observed in additively manufactured materials [21]. No observable differences between samples were detected, though.

Similar solidification fronts were observed in examined samples of moderate non-orthogonal configurations. They all exhibited a radial symmetry which originated in the top center region of the beads. Columnar structures were detected at the outer edges of the bead, more specifically at the bead-substrate interface, while more equiaxed and cellular structures/sub-grains were observed closer to the center of the beads. This can possibly be due to slightly elevated solidification rates as the heat transfer is directed

radially outward toward the substrate. Such solidification microstructure is a common observance in DED-processed materials [22].

For more extreme non-orthogonal depositions where penetration depths were very shallow, it can be observed that columnar structures dominated the microstructure. This can be due to the reduced substrate-bead interface perimeter as compared to samples with a larger penetration depth and thus a larger interface perimeter due to the circular shape of the perimeter. With a reduced perimeter, the heat-sinking effect of the substrate was diminished, therefore reducing the solidification rates experienced and thus only producing columnar structures, irrespective of the bead heights and widths

Fig. 10 Grain morphology representation of bead depositions with penetration depths < 20 μm. **A** $\theta = 45^\circ$; $\beta = 15^\circ$. **B** $\theta = 135^\circ$; $\beta = 15^\circ$. **C** $\theta = 45^\circ$; $\beta = 45^\circ$. **D** $\theta = 135^\circ$; $\beta = 45^\circ$. Columnar structures dominate beads with shallow penetration depths



involved. This highlights the primary role penetration depth plays in solidification phenomena during deposition.

In the wire-DED comparative study, the dilution region was preferentially positioned away from the

bead center in the pure lead (right of the bead center) and pure lean (left of the bead center) configurations. Such dilution profile variations can be attributed to variations in the maximum laser intensity location within the melt pool. It can also be attributed to the variations in laser intensity and wire location within the elongated laser beam diameter in non-orthogonal configurations. The observed asymmetry in the orthogonal configuration can be attributed to the wire feed not being consistently straight as it exits the contact tip; moreover, the contact tip is 16° off from the normal, which can add variability feed at the exit of the contact tip. Further examination of this phenomenon is warranted for future studies. A significantly different dilution profile was observed in the [$\theta = 105^\circ$; $\beta = 0^\circ$] pure lead angle configuration. Maximum penetration, though relatively small, was observed toward the rightmost and leftmost corners of the bead. Such a penetration depth profile is observed in AM samples exhibiting a sickle-like temperature distribution on the surface of the melt pool, typically resulting when process parameters exceed the evaporation temperature of the material. Consequently, the minimum penetration depth is observed at the center due to a comparatively lower temperature due to this sickle-like temperature distribution profile [23]. This indicates that this angular configuration represents a potential upper limit from a process-structure relation standpoint.

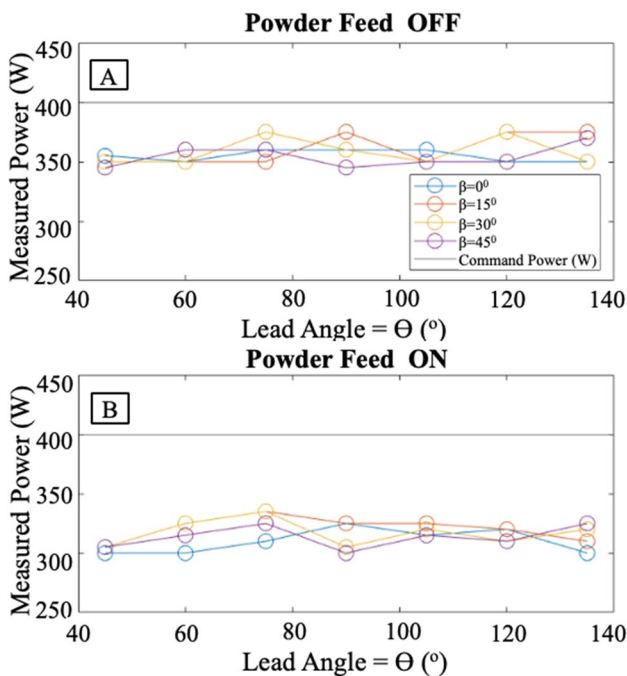
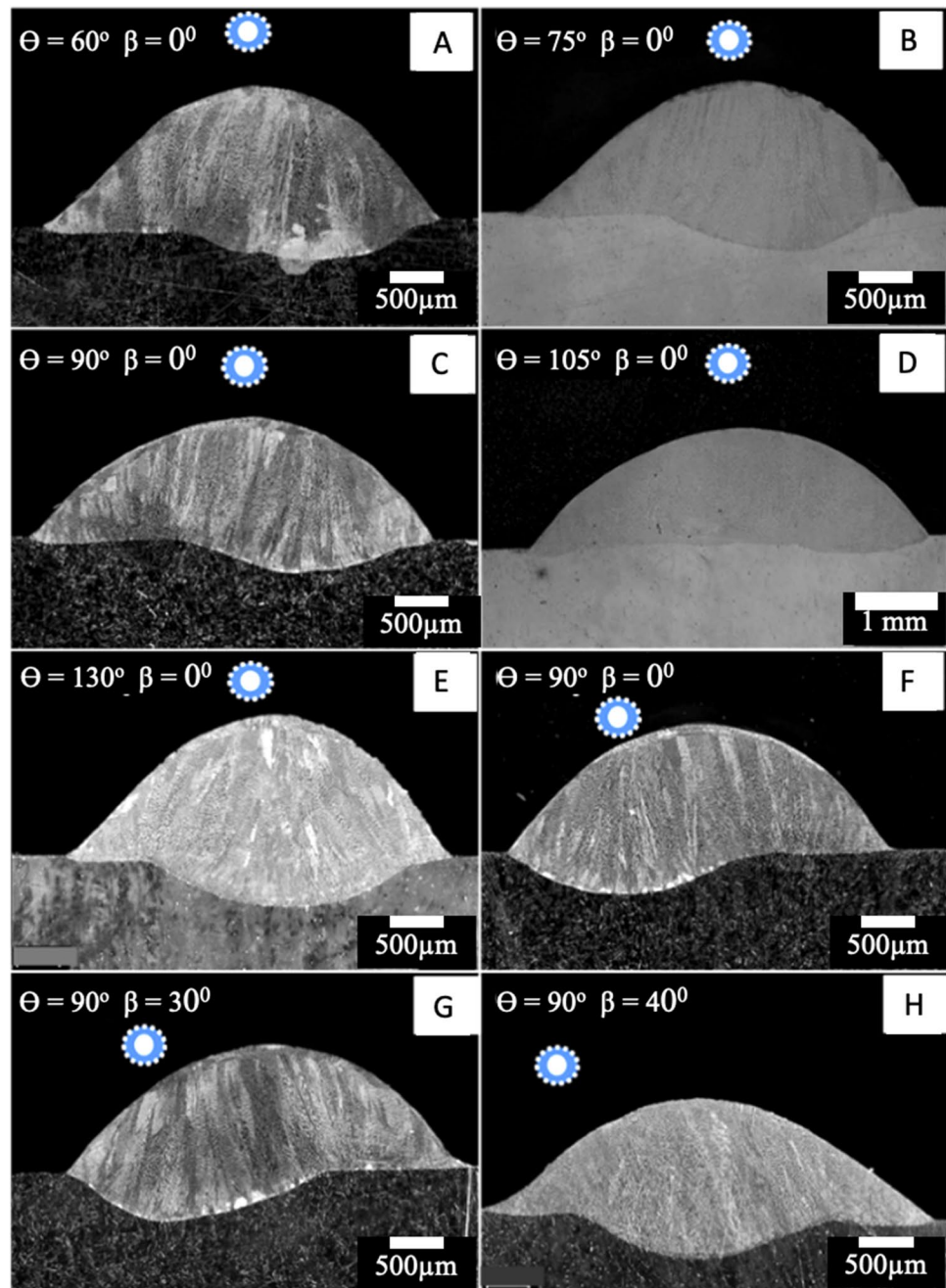


Fig. 11 Laser attenuation quantitative measurements. **A** Powder feed turn off. **B** Powder feed turn on. There are slight differences between varying laser incidence angles with powder feed turned ON and OFF. Laser attenuation is more pronounced when the powder feed is turned ON as compared to when it is turned OFF, though

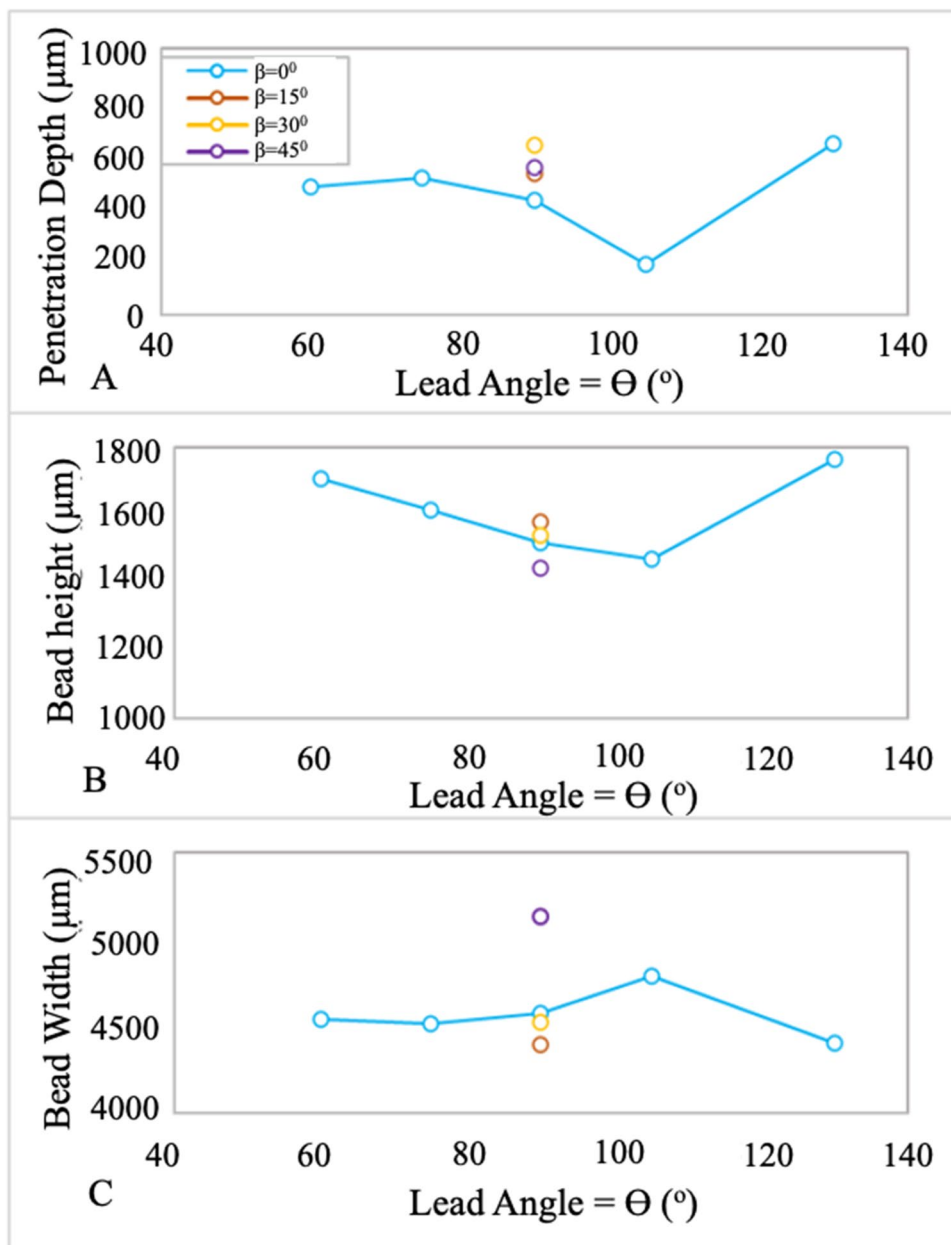
Fig. 12 Micrographs of wire-feed DED samples, where **A** $\Theta = 60^\circ$; $\beta = 0^\circ$. **B** $\Theta = 75^\circ$; $\beta = 0^\circ$. **C** $\Theta = 90^\circ$; $\beta = 0^\circ$. **D** $\Theta = 105^\circ$; $\beta = 0^\circ$. **E** $\Theta = 130^\circ$; $\beta = 0^\circ$. **F** $\Theta = 90^\circ$; $\beta = 15^\circ$. **G** $\Theta = 90^\circ$; $\beta = 30^\circ$. **H** $\Theta = 90^\circ$; $\beta = 40^\circ$. Dotted and solid circles represent the position of laser and direction of wire-feed for corresponding angular setting



The observed Bell (bead width) and inverse Bell curve (bead height, penetration depth) behavior for the geometric characteristics, with the maximum and minimum points (respectively) at a lead angle of 105° , indicates that there is an ability to adjust bead geometry by modifying lead angle. Note that, unlike powder-feed systems, wire-feed systems exhibit very high material retention

efficiency within the melt pool. Consequently, samples processed with equivalent laser energy densities and wire feed rates should result in highly similar volumetric bead geometries. This can be compared to powder-DED, which produced samples with progressively diminished bead geometries with more extreme non-orthogonal angular configurations.

Fig. 13 Effect of lead and lean angles on the bead morphology in the wire-feed DED method depositions

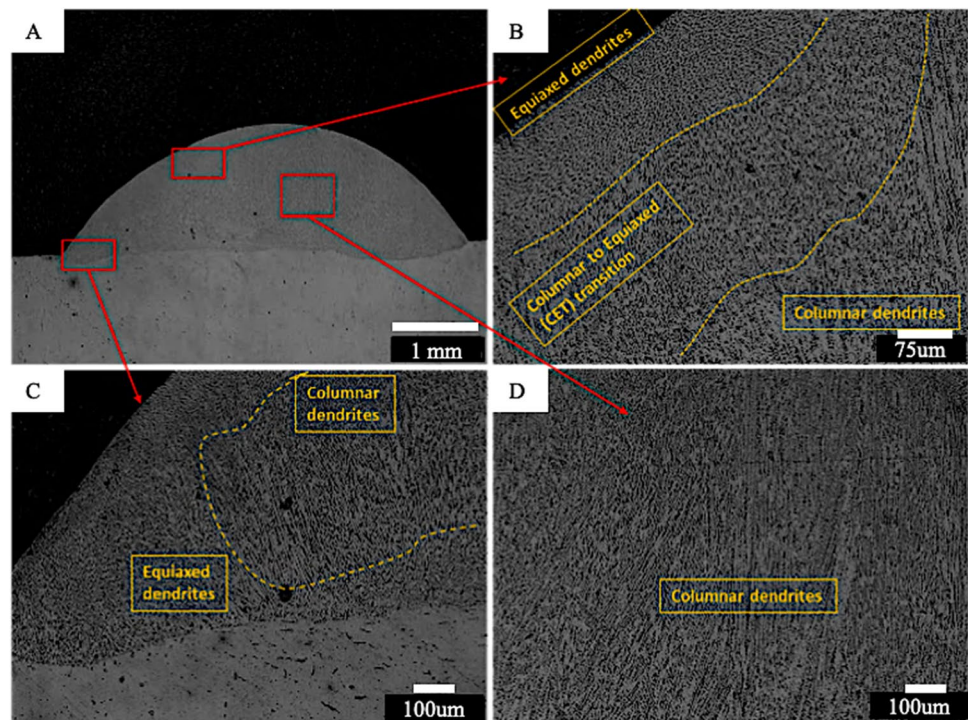


5 Conclusions

This study examined the effects of laser incidence angle on bead morphology, phase composition, textural representation, bead microstructure, and resultant power losses. The following conclusions were resultant:

1. The ricochet effect, extent of absorbed reflected energy, and resultant powder catchment efficiency play an integral role in bead geometry generation. Acute lead angles exhibited more prominent characteristics due to the presence of the previously deposited material in the wake of the deposition front, acting as a barrier to ricocheted particles and thus enhancing powder catchment.
2. A larger lean angle, irrespective of the lead angle, resulted in smaller bead deposits. Furthermore, a pure lean angle of 45° resulted in significantly smaller bead sizes due to the greatly diminished powder catchment efficiency.
3. Austenitic FCC phases were observed in both unprocessed powders and the processed samples, with diffraction patterns exhibiting potential texture in the 111 and 200 planes and some peak broadening rep-

Fig. 14 A Micrograph of the [$\theta = 105^\circ$; $\beta = 0^\circ$] pure lead sample. High magnification images showing the grain structure at the **B** top, **C** bottom, and **D** center of the bead



representative of residual stress present in the samples. Minor differences between the samples were observed, though.

4. Significant fibrous and other localized textures were present, indicating the presence of columnar/dendritic and equiaxed/cellular structures, respectively. Minor textural differences between samples were observed.
5. No significant differences in microstructural composition or grain size were detected with varying incidence angles at moderate non-orthogonal angles. Equivalent solidification microstructure was observed, with grain size variations remaining within the 1–1.5 and 2–2.5 μm ranges both within and across beads, respectively.
6. Penetration depth plays an integral role in the governing solidification phenomena and consequent microstructure, with shallow penetration depths (< 20 μm) resulting in predominantly columnar structures form due to a reduced bead-substrate interface perimeter and thus less pronounced heat sinking effect by the substrate, irrespective of the bead heights and/or widths. In contrast, deeper penetration depths r in columnar structures to form at the interface, while more equiaxed structures form at the bead center.
7. Dilution profiles were found to be asymmetric in both orthogonal and non-orthogonal wire DED samples.

8. No significant microstructural differences were observed between powder-fed and wire-fed samples, indicating that similar solidification phenomena govern both hybrid manufacturing techniques.

The results obtained in this study provided valuable insight into the underlying phenomena at play with regard to non-orthogonal deposition operations. In order to build upon such knowledge, a few recommended potential studies can be conducted to bring the non-orthogonal deposition techniques closer to becoming industrially implementable.

- 1) An examination of modified process parameters can be conducted to produce consistent bead geometries, irrespective of the employed angular configuration.
- 2) The incorporation of continuously changing angular configurations can give some insight into the effects on bead characteristics in curved surfaces.
- 3) Modeling and simulation experiments can be used to develop a more in-depth, theoretical understanding of the phenomena at play here as well, which can be validated via advanced experimental setups.

Acknowledgements The authors would like to acknowledge the cooperation and support of the Mazak Corporation and Autodesk. The authors would also like to acknowledge Dennis Brown, and Matt Sallas for their contributions.

Author contribution Omar Elsayed: Conceptualization, data curation, formal analysis, project administration, and writing (original draft); Venkata Surya Karthik Adapa: conceptualization, data curation, formal analysis, and writing (original draft); Samuel Kersten, Derek Vaughan, Christopher Masuo, Myong Joon Kim, Thomas Feldhausen, and Thomas Kurfess: data curation and investigation; Christopher Saldana: conceptualization, project administration, supervision, and writing (review and editing).

Funding We would also like to thank the Department of Energy for funding this work via DE-EE0008303. This work was supported by the US Department of Energy, Office of Energy Efficiency and Renewable Energy, Advanced Manufacturing Office, under contract number DE-AC05-00OR22725.

Declarations

Conflict of interest The authors declare no competing interests.

References

- Zhu Z, Dhokia VG, Nassehi A, Newman ST (2013) A review of hybrid manufacturing processes – state of the art and future perspectives. *Int J Comp Integ Manuf* 26(7):596–615. <https://doi.org/10.1080/0951192X.2012.749530>
- Wilson JM, Piya C, Shin YC, Zhao F, Ramani K (2014) Remanufacturing of turbine blades by laser direct deposition with its energy and environmental impact analysis. *J Cleaner Prod* 80:170–178. <https://doi.org/10.1016/j.jclepro.2014.05.084>
- Elser A, Königs M, Verl A, Servos M (2018) On achieving accuracy and efficiency in additive manufacturing: requirements on a Hybrid CAM System. In: *Procedia CIRP*, 51st CIRP Conference on Manufacturing Systems, vol 72, pp 1512–1517. <https://doi.org/10.1016/j.procir.2018.03.265>
- Kumbhar NN, Mulay AV (2018) Post processing methods used to improve surface finish of products which are manufactured by additive manufacturing technologies: a review. *J Inst Engineers (India): Series C* 99(4):481–487. <https://doi.org/10.1007/s40032-016-0340-z>
- Lasemi A, Xue D, Peihua G (2010) Recent development in CNC machining of freeform surfaces: a state-of-the-art review. *Comp-Aided Des* 42(7):641–654. <https://doi.org/10.1016/j.cad.2010.04.002>
- Kim M-s, Wook-jin O, Baek G-y, Jo Y-k, Lee K-y, Park S-h, Shim D-s (2020) Ultrasonic nanocrystal surface modification of high-speed tool steel (AISI M4) layered via direct energy deposition. *J Mat Proc Technol* 277:116420. <https://doi.org/10.1016/j.jmatp.2019.116420>
- Lin J (2000) Laser attenuation of the focused powder streams in coaxial laser cladding. *J Laser Appl* 12(1):28–33. <https://doi.org/10.2351/1.521910>
- Grasso M, Demir AG, Previtali B, Colosimo BM (2018) In situ monitoring of selective laser melting of zinc powder via infrared imaging of the process plume. *Robotics and Comp-Integr Manuf* 49:229–239. <https://doi.org/10.1016/j.rcim.2017.07.001>
- Fu Y, Loredo A, Martin B, Vannes AB (2002) A theoretical model for laser and powder particles interaction during laser cladding. *J Mat Proc Technol* 128(1):106–112. [https://doi.org/10.1016/S0924-0136\(02\)00433-8](https://doi.org/10.1016/S0924-0136(02)00433-8)
- Liu J, Li L, Zhang Y, Xie X (2005) Attenuation of laser power of a focused Gaussian beam during interaction between a laser and powder in coaxial laser cladding. *J Phys D: Appl Phys* 38(10):1546–1550. <https://doi.org/10.1088/0022-3727/38/10/008>
- Pinkerton AJ (2007) An analytical model of beam attenuation and powder heating during coaxial laser direct metal deposition. *J Phys D: Appl Phys* 40(23):7323–7334. <https://doi.org/10.1088/0022-3727/40/23/012>
- Hao J, Meng Q, Li C, Li Z, Dazhong W (2019) Effects of tilt angle between laser nozzle and substrate on bead morphology in multi-axis laser cladding. *J Manufac Proc* 43:311–322. <https://doi.org/10.1016/j.jmapro.2019.04.025>
- Abrams H (1971) Grain size measurement by the intercept method. *Metallography* 4(1):59–78. [https://doi.org/10.1016/0026-0800\(71\)90005-X](https://doi.org/10.1016/0026-0800(71)90005-X)
- Macken Instruments Inc (2020) “P2000Y”. <https://www.macken.com/products/p2000y>
- Liao Y-C, Ming-Huei Y (2007) Effects of laser beam energy and incident angle on the pulse laser welding of stainless steel thin sheet. *J Mat Proc Technol* 190(1):102–108. <https://doi.org/10.1016/j.jmatprotec.2007.03.102>
- Haley JC, Schoenung JM, Lavernia EJ (2018) Observations of particle-melt pool impact events in directed energy deposition. *Addi Manufac* 22:368–374. <https://doi.org/10.1016/j.addma.2018.04.028>
- Prasad S, Himani FB, Kaplan AFH (2020) Powder incorporation and spatter formation in high deposition rate blown powder directed energy deposition. *Addi Manufac* 35:101413. <https://doi.org/10.1016/j.addma.2020.101413>
- Costello AC, Koduri SK, Sears JW (2003) Optimization of laser powder deposition for 316L stainless steel. *Int Cong Appl Lasers & Electro-Optics* 2003(1):701. <https://doi.org/10.2351/1.5060072>
- Shuro I, Kobayashi S, Nakamura T, Tsuzaki K (2014) Determination of α/γ phase boundaries in the Fe–Cr–Ni–Mn quaternary system with a diffusion-multiple method. *J Alloys and Compounds* 588:284–289. <https://doi.org/10.1016/j.jallcom.2013.11.095>
- Lee JH, Kim YS (2015) Intergranular corrosion of 316L stainless steel by aging and UNSM (ultrasonic nano-crystal surface modification) treatment. *Corrosion Sci Technol* 14(6):313–324. <https://doi.org/10.14773/cst.2015.14.6.313>
- Basak A, Das S (2016) Epitaxy and microstructure evolution in metal additive manufacturing. *Ann Rev Mat Res* 46(1):125–149. <https://doi.org/10.1146/annurev-matsci-070115-031728>
- Saboori A, Gallo D, Biamino S, Fino P, Lombardi M (2017) An overview of additive manufacturing of titanium components by directed energy deposition: microstructure and mechanical properties. *Appl Sci* 7(9):883. <https://doi.org/10.3390/app7090883>
- Zhong C, Pirch N, Gasser A, Poprawe R, Schleifenbaum JH (2017) The influence of the powder stream on high-deposition-rate laser metal deposition with Inconel 718. *Metals* 7(10):443. <https://doi.org/10.3390/met7100443>

Publisher’s note Springer Nature remains neutral with regard to jurisdictional claims in published maps and institutional affiliations.

Springer Nature or its licensor (e.g. a society or other partner) holds exclusive rights to this article under a publishing agreement with the author(s) or other rightsholder(s); author self-archiving of the accepted manuscript version of this article is solely governed by the terms of such publishing agreement and applicable law.